Baker *et al.*, *Ecol. Monogr.* **66**, 203 (1996); R. G. Baker *et al.*, *Geology*, in press.

14. H. Zhu and R. G. Baker, *J. Paleolimnol.* **14**, 337 (1995).
15. E. Grüger, *Quat. Res.* **2**, 217 (1972).
16. At Pittsburg Basin (*15*), for example, the pollen sequence starts with a northern conifer assemblage (spruce, pine, fir, and larch), possibly representing the late-Illinoian glacial transition to the Sangamon interglacial. There follows a tripartite section in which the first and third zones are dominated by temperate hardwoods such as oak, hickory, elm, beech, walnut, and sweetgum and the middle zone by grasses, ragweed, and chenopods along with oak and other temperate hardwoods, a typical prairie-border or savanna assemblage. After an abrupt termination that probably represents a hiatus, the pollen is dominated by prairie-type taxa, leading up to a pine/birch zone and finally a spruce zone.
17. During the forest period from 55 to 25 ka, significant $\delta^{13}C$ excursions to more negative values culminate at ~52 and ~46 ka. These features may represent differences in the "openness" of the forest environment. Studies of modern closed-canopy forests have revealed that the increased recycling of plant-respired CO_2 [E. Medina, L. Sternberg, E. Cuevas, *Oecologia* **87**, 369 (1991)] and reduced light intensities [J. R. Ehleringer *et al.*, *ibid.* **70**, 520 (1986)] tend to shift plant tissues toward more negative $\delta^{13}C$ values when compared to a more open setting. One hallmark of the late-glacial boreal forests of the Midwest was their relative "openness," as suggested by their inclusion of shade-intolerant herbs like *Artemisia* and *Ambrosia* [D. C. Amundson and H. E. Wright Jr., *Ecol. Monogr.* **49**, 153 (1979)]. Thus, in addition to the physical controls of the forest canopy on understory $\delta^{13}C$ values, some opportunity for C_4 plant habitation may have also existed during the more "open" forest periods, reinforcing the trend toward less negative $\delta^{13}C$ values. Whether the collective consideration of these factors can be translated to a glacial-period forest dominated by conifers versus deciduous trees remains unclear.
18. W. Dansgaard, *Tellus* **16**, 438 (1964).
19. G. W. Moore and G. N. Sullivan, *Speleology*, (Zephyrus Press, Teaneck, NJ, ed. 2, 1978), p. 150.
20. This scenario neglects $\delta^{18}O$ variation of ocean water that occurred as ice volume fluctuated; including this factor would increase the temperature range estimate to more than 4°C.
21. I. Friedman, J. R. O'Neil, M. Fleischer, *U.S. Geol. Surv. Prof. Pap. 440-KK* (1977).
22. W. H. Johnson and L. R. Follmer, *Quat. Res.* **31**, 319 (1989).
23. B. B. Curry and L. R. Follmer, in *The Last Interglacial-Glacial Transition in North America*, P. U. Clark and P. D. Lea, Eds., *Geol. Soc. Am. Spec. Pap. 270* (1992), pp. 71–88.
24. D. S. Leigh, *Geol. Soc. Am. Bull.* **106**, 430 (1994).
25. ⸻ and J. C. Knox, *Quat. Res.* **39**, 282 (1993); B. B. Curry and M. J. Pavich, *ibid.* **46**, 19 (1996).
26. S. L. Forman *et al.*, *Palaeogeogr. Palaeoclimatol. Palaeoecol.* **93**, 71 (1992).
27. G. R. Whittecar and A. M. Davis, *Quat. Res.* **17**, 228 (1982).
28. E. A. Bettis III *et al.*, in *Iowa Geol. Surv. Bur. Guideb. Ser. No. 18* (1996), pp. 95–98; B. B. Curry, *Quat. Res.* **50**, 128 (1998).
29. D. G. Martinson *et al.*, *Quat. Res.* **27**, 1 (1987).
30. G. Bond *et al.*, *Nature* **365**, 143 (1993).
31. A. Baker, P. L. Smart, R. L. Edwards, *Geology* **23**, 309 (1995).
32. A. Berger and M. F. Loutre, *Quat. Sci. Rev.* **10**, 297 (1991).
33. We thank P. Hauck, G. Osburn, R. Young, and J. Morris for caving assistance and J. Hoff, H. Cheng, C. Borton, and R. McEwan for laboratory assistance. Reviews by H. E. Wright Jr. and D. A. Richards and discussions with E. C. Alexander Jr. helped improve the manuscript. Supported by NSF grants to R.L.E., E.I., and L.A.G. J.A.D. was supported by NSF-sponsored Research Training (to M. Davis) and Graduate Research Training (to M. Person) grants and a Geological Society of America student research grant.

16 July 1998; accepted 29 Octoer 1998

Oxygen Isotope Exchange Between Refractory Inclusion in Allende and Solar Nebula Gas

Hisayoshi Yurimoto,* Motoo Ito, Hiroshi Nagasawa

A calcium-aluminum–rich inclusion (CAI) from the Allende meteorite was analyzed and found to contain melilite crystals with extreme oxygen-isotope compositions (~5 percent oxygen-16 enrichment relative to terrestrial oxygen-16). Some of the melilite is also anomalously enriched in oxygen-16 compared with oxygen isotopes measured in other CAIs. The oxygen isotopic variation measured among the minerals (melilite, spinel, and fassaite) indicates that crystallization of the CAI started from oxygen-16–rich materials that were probably liquid droplets in the solar nebula, and oxygen isotope exchange with the surrounding oxygen-16–poor nebular gas progressed through the crystallization of the CAI. Additional oxygen isotope exchange also occurred during subsequent reheating events in the solar nebula.

Calcium-aluminum–rich inclusions (CAIs) are millimeter- to centimeter-sized objects composed of refractory minerals in chondrites and are widely believed to be the first solid particles formed in the solar nebula. The texture and composition of CAIs suggest that they were exposed to high temperatures, possibly during the infall phase that formed the sun and the solar nebula (*1*). Thus, CAIs were once molten or partially molten in the solar nebula. The crystallization sequence for a Ca-Al–rich silicate liquid is spinel, melilite, anorthite, and fassaite (*2*), and these minerals usually coexist in CAIs (*3*). Trace element distributions among the minerals is consistent with crystallization from a liquid state under assumed nebular conditions (*4*). If the constituent minerals were sequentially crystallized from such a liquid in an unchanging nebular environment, then the isotopic compositions of the minerals will be identical. However, oxygen isotope ratios are variable among the CAI minerals (*5*, *6*).

In a three-isotope diagram, oxygen isotope ratios of CAI minerals, in general, are distributed along an ^{16}O component–enriched line called the carbonaceous chondrite anhydrous minerals (CCAM) line. The minerals at early- and late-crystallization stages are enriched in ^{16}O (spinel, $\delta^{17 \text{ or } 18}O_{SMOW} \sim -40$ per mil; fassaite, $\delta^{17 \text{ or } 18}O_{SMOW} = -20$ to -40 per mil) (*7*), whereas those at intermediate crystallization stages are less enriched in ^{16}O (melilite and anorthite, $\delta^{17 \text{ or } 18}O_{SMOW} \sim 0$ per mil) (*6*). Although diffusive exchange

after the crystallization of CAIs may explain the oxygen isotope heterogeneity (*8*), recent diffusion studies indicate that it is difficult to explain the observed O isotope distribution among CAI minerals by solid-gas diffusive exchange (*9*).

Recently a CAI containing ^{16}O-rich melilite in an ordinary chondrite was reported (*10*). The similarity of O isotopic composition between CAIs of carbonaceous and of ordinary chondrites suggests that they are genetically related and that CAI precursors were enriched in ^{16}O (*8*). On the basis of these measurements, the genetic link between the heterogeneous O isotope distribution among the constituent minerals and the igneous textures of CAIs has not been explained. Studies of the O isotope microdistribution within and among minerals may help to develop a model for the formation of the CAIs that explains their texture and O isotopic composition (*11*). Here we report on O isotopic evidence for the genesis of CAIs found in the Allende carbonaceous chondrite.

CAI 7R-19-1 was collected from the Allende CV3 chondrite, but the CAI is incomplete because of fragmentation during laboratory preparation. The CAI is round, and its diameter is estimated to be ~5 mm from the curvature of the CAI edge (Fig. 1). The CAI consists mainly of melilite (~70 volume %), fassaite (~15 volume %), and spinel (~10 volume %) grains. Minor mineral phases are hibonite and $CaTiO_3$ perovskite. Alteration products (anorthite; An_{99}, grossular) are present mainly along some grain boundaries between the major minerals. The melilite crystals have uniform or weakly zoned cores ($Åk_{13-20}$) and zoned rims ($Åk_{20-50}$) (Fig. 2). The large angular fassaite crystals usually have sector zoning and have a composition with a range of 11 to 16 weight % ($TiO_2 + Ti_2O_3$) and 17 to 22 weight % Al_2O_3. Small, rounded fassaite grains are observed within the melilite grains.

H. Yurimoto, Department of Earth and Planetary Sciences, Tokyo Institute of Technology, Ookayama, Meguro, Tokyo 152-8551, Japan. M. Ito and H. Nagasawa, Department of Chemistry, Gakushuin University, Mejiro, Toshima, Tokyo 171-8588, Japan.

*To whom correspondence should be addressed. E-mail: yuri@geo.titech.ac.jp

The compositions of the small fassaite grains are within the composition range of the large angular fassaite. The spinel is nearly pure $MgAl_2O_4$. Chondrite-normalized patterns of trace elements for melilite and fassaite show complementary distribution (Fig. 3), resembling those of type-B CAIs (4). The petrographic texture and mineral compositions of 7R-19-1 may correspond to those of coarse-grained melilite-rich type B or fassaite-rich compact type A CAIs (3, 12). The igneous textures suggest that 7R-19-1 was crystallized from a molten state and thus represents a primary CAI.

A fragment from the center part of 7R-19-1 was polished and prepared for in situ O isotope analysis by secondary ion mass spectrometry (SIMS) (13). The locations of the analyses are shown in Fig. 1 and the results are listed in Table 1. The results are plotted in a three-isotope diagram (Fig. 4). The analyses lie along the CCAM line and are consistent with previous observations of normal coarse-grained CAIs. However, in 7R-19-1, all three minerals have large negative $\delta^{17}O$ and $\delta^{18}O$ anomalies with the order spinel or melilite >fassaite >melilite, in contrast to those generally observed for normal CAIs, spinel >fassaite >melilite. The average $\delta^{17 \text{ or } 18}O_{SMOW}$ value is -38 per mil and -36 per mil for the melilite grain, Mel* (Fig. 1), and -12 per mil and -10 per mil for the melilite grain, Mel (Fig. 1), respectively. This is the first observation that melilite grains with and without ^{16}O-enrichment are directly in contact with each other in the same CAI (14).

Spinel crystals and several small, rounded crystals of fassaite (<20 μm in diameter) are scattered in the ^{16}O-rich melilite crystals. The textural relations indicate that the spinel crystals were the first crystallizing minerals in the CAI, and these grains continued to crystallize during crystallization of the ^{16}O-rich melilite. The fassaite grains appear to have been trapped in the melilite and, because of their rounded shapes, may be a relict phase of the CAI precursor. All the spinel grains and the small fassaite grains are enriched in ^{16}O to the same degree as those of the surrounding ^{16}O-rich melilite. This indicates that the CAI was primarily enriched in ^{16}O. These O isotopic characteristics observed for 7R-19-1 are also consistent with simple solidification of Ca-Al–rich liquid on the basis of the experimentally determined crystallization sequence (2).

We found one melilite crystal, Mel, whose O isotope composition is similar to that of
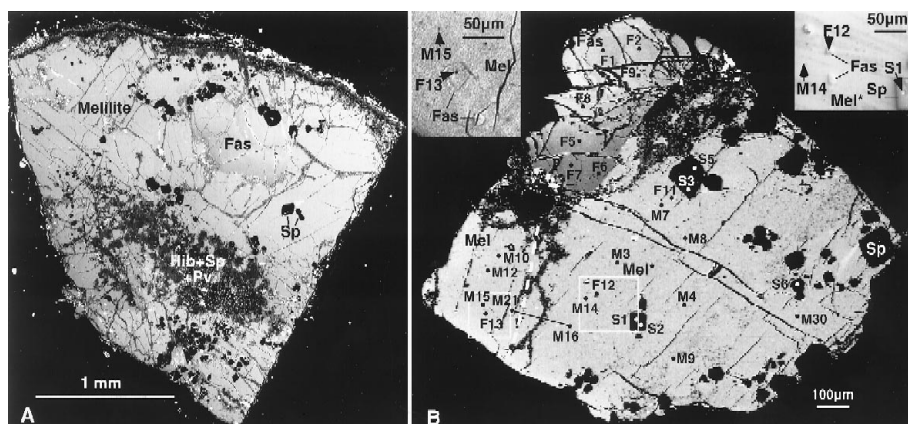
Fig. 1. (A) Backscattered electron image (BEI) of the largest fragment of 7R-19-1 CAI from the Allende meteorite, 7R-19-1(d). The CAI is surrounded by a spinel- and perovskite-rich rim. **(B)** BEI of another 7R-19-1 fragment used for O isotope analyses, 7R-19-1(a). This fragment was collected from the central part of the CAI. Sp, spinel; Mel*, ^{16}O-rich melilite; Mel, ^{16}O-poor melilite; Fas, fassaite; Hib, hibonite; Pv, perovskite. The grain boundary between Mel* and Mel grains is shown by a dotted line. Circles show locations of the SIMS analysis with the analysis number given in Table 1. The insets at the upper left and upper right are a BEI and a microphotograph under reflected light, corresponding to the areas near analytical locations of F13 and F12, respectively, showing some of the sputtering craters formed by SIMS. The straight line connecting analytical locations of M16 and M21 corresponds to line analyses in Fig. 2.

Fig. 2. Distribution of åkermanite contents (mol %) and oxygen isotope ratios along the line between analytical locations at M16 and M21 of Fig. 1. Open and solid circles are $\delta^{17}O_{SMOW}$ and $\delta^{18}O_{SMOW}$ values, respectively. Size of the symbols corresponds to the primary beam diameter analyzed (3 μm). Error bars are 1σ. Lines and boxes are averages and 1σ reproducibility of $\delta^{18}O_{SMOW}$ within the O isotopic ratio homogeneous area, respectively. The region enriched in ^{16}O sharply contacts the ^{16}O-poor region, whereas an obvious åkermanite content gap is not observed at the contact. The åkermanite content increases near and at the grain boundary. Other abbreviations are the same as in Fig. 1.
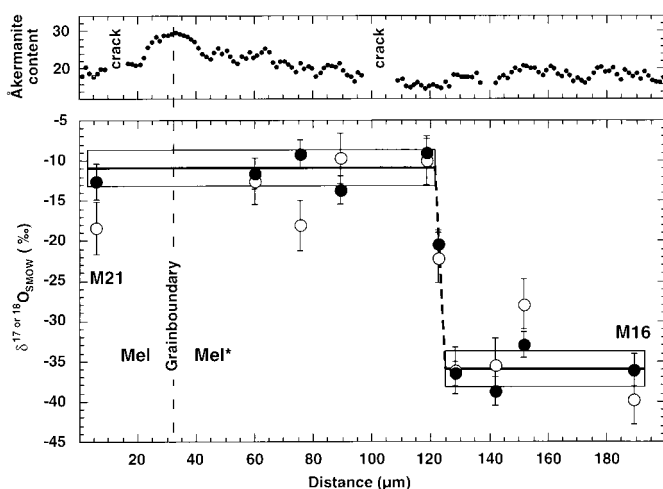
Table 1. Oxygen isotopic data for the 7R-19-1 CAI. All errors are 1σ.

Analysis number	$\delta^{17}O_{SMOW}$ (per mil)	$\delta^{18}O_{SMOW}$ (per mil)
^{16}O-enriched melilite (Mel*)		
M3	-33.0 ± 3.0	-34.0 ± 2.0
M4	-31.3 ± 3.0	-32.9 ± 2.0
M7	-37.7 ± 3.2	-28.9 ± 2.2
M8	-42.3 ± 3.1	-33.6 ± 2.1
M9	-29.0 ± 2.8	-31.7 ± 2.1
M14	-40.3 ± 3.0	-43.9 ± 1.9
M16	-39.8 ± 3.0	-36.1 ± 1.9
M30	-48.2 ± 2.9	-44.2 ± 2.3
Small fassaite inclusions		
F11	-32.2 ± 3.1	-33.6 ± 2.0
F12	-37.8 ± 3.0	-36.3 ± 2.0
Normal melilite (Mel)		
M10	-4.1 ± 3.5	-9.8 ± 1.8
M12	-13.4 ± 3.2	-9.6 ± 2.1
M15	-10.4 ± 3.2	-8.1 ± 2.1
M21	-18.4 ± 3.2	-12.5 ± 2.2
Small fassaite inclusion		
F13	-16.9 ± 3.3	-16.5 ± 2.1
Angular fassaite		
F1	-9.3 ± 2.8	-9.6 ± 2.1
F2	-5.2 ± 2.9	-12.6 ± 2.0
F5	-24.3 ± 3.0	-18.5 ± 2.1
F6	-17.1 ± 3.4	-11.7 ± 2.1
F7	-21.4 ± 3.4	-21.8 ± 2.1
F8	-5.5 ± 2.5	-2.3 ± 2.1
F9	0.2 ± 3.0	-1.3 ± 2.0
Spinel		
S1	-41.1 ± 3.3	-39.0 ± 1.8
S2	-34.3 ± 3.0	-35.3 ± 2.0
S3	-37.8 ± 2.8	-35.3 ± 2.1
S5	-41.0 ± 2.9	-39.5 ± 2.2
S6	-38.0 ± 3.0	-40.2 ± 2.1

melilites found in normal CAIs. This ^{16}O-poor melilite crystal includes some small-grained (<30 μm in diameter) fassaite, like the adjacent ^{16}O-rich melilite. However, the fassaite grain showed an O isotopic composition enriched in ^{16}O ($\delta^{17 \text{ or } 18}O_{SMOW}$ = −17 per mil), which is different from that of the surrounding ^{16}O-poor melilite. The degree of enrichment of ^{16}O is less than those of the ^{16}O-rich melilite and the small-grained fassaite found therein, and is similar to those of the large angular fassaite grains (Fig. 1). The similarity in the O isotopic composition between the small-grained fassaite in the ^{16}O-poor melilite and the angular fassaite suggests that the angular fassaite and the small-grained fassaite in the ^{16}O-poor melilite crystallized before the ^{16}O-poor melilite crystallized.

Oxygen isotope zoning along the CCAM line (−25 < $\delta^{17 \text{ or } 18}O_{SMOW}$ < 0 per mil) was observed in an angular fassaite crystal. The observed zoning of O isotopes cannot be explained by solid-state diffusion of O after crystallization of the fassaite. If this zoning occurred by diffusion of O with ^{16}O-poor composition in the surrounding gaseous reservoir, then the adjacent melilite crystal with higher diffusivity (9) could not have retained its ^{16}O-rich composition. Therefore, the observed zoning in the angular fassaite indicates that the O isotope composition changed during the crystallization of the fassaite. Moreover, because the ^{16}O-rich and ^{16}O-poor melilite grains are in direct contact with each other, solid-state diffusion as a principal mechanism to generate the O isotopic heter-

ogeneity between the Mel* and the Mel grains is ruled out. The O isotope ratios of the Mel* grain change from ^{16}O-rich to ^{16}O-poor at the boundary between the core and the surrounding zoned rim (Fig. 2). The O isotopic composition of normal zoned rim is ^{16}O-poor to the same degree as those of the adjacent Mel grain. This indicates that the ^{16}O-rich melilite crystallized before the ^{16}O-poor melilite.

From the O isotopic distribution among the minerals and the petrographic texture, the crystallization sequence of the 7R-19-1 CAI may be traced as follows: spinel crystallized first, and then melilite crystallized in an environment enriched in ^{16}O by ~5% relative to the terrestrial isotope ratio. After spinel and melilite, fassaite started to crystallize. If 7R-19-1 crystallized from a melt, the O isotope composition of the liquid should become ^{16}O-poor during cooling and this change should be recorded in the minerals, especially in the O isotopic variation of fassaite. The degree of ^{16}O excess in the CAI minerals reflects the exchange rate between ^{16}O-poor surrounding nebular gas and ^{16}O-rich CAI melt.

After the fassaite crystallized, the ^{16}O-poor melilite crystallized. Because the chemical compositions of the core of the ^{16}O-poor melilite and of the adjacent ^{16}O-rich melilite are similar (Åk_{15-20}) and the O isotopic distribution changes from ^{16}O rich to ^{16}O poor (Fig. 2), it is difficult to understand how the ^{16}O-poor melilite was sequentially crystal-

lized by a single stage of cooling. Therefore, the ^{16}O-poor melilite crystallization probably occurred by reheating of the CAI in the solar nebula. Because solid-state diffusion is not plausible as the principal mechanism of O isotopic exchange between the two melilite grains, possible candidates for the mechanism may be metamorphic recrystallization and crystallization after remelting of precursor materials with ^{16}O-rich composition (probably $\delta^{17 \text{ or } 18}O_{SMOW}$ ~ −40 per mil) during subsequent reheating events.

Although metamorphic recrystallization of melilite in CAI systems has not been well studied, evidence of metamorphism has been reported from Allende type B CAIs (15). One potential problem with the remelting model is that fassaite grains should melt first and exchange oxygen isotopes rather than melilite grains, according to the phase equilibrium diagram of the CAI composition. However, for transient heating, melting of minerals may be controlled by kinetics rather than equilibrium. According to a model for the kinetics of congruent melting, the melting rate of åkermanite is much faster than that of diopside at the same temperature above the melting temperature of åkermanite (16). Because grain sizes of melilite are similar to those of angular fassaite, melilite grains may be melted faster than the fassaite grains. After the transient heating, melilite or fassaite grains, or both, were again crystallized from the remelted liquid. Trace element distribution among the minerals (Fig. 3) and similar åkermanite contents between ^{16}O-rich and ^{16}O-poor melilite grains are consistent with such partial remelting.

All of the O isotope ratios observed in 7R-19-1 lie along the CCAM line, and the lower limit value of ^{16}O enrichment among minerals is −48 per mil, indicating that the basic O isotope ratios are similar to normal CAIs in carbonaceous chondrites. These indicate that the degree of enrichment of ^{16}O is variable among minerals in individual CAIs. Therefore, the formation process we infer for 7R-19-1 may be applicable to other CAIs. If CAI precursors were originally composed of ^{16}O-rich materials, remelting or metamorphism by reheating events may enhance the O isotopic exchange between the ambient nebular gas and the newly crystallized minerals. If the reheating event occurred one or more times during CAI formation, the O isotopic composition of CAIs can be reset to the solar nebula value except for grains that did not remelt. The heterogeneous O isotopic distribution among minerals having igneous textures like normal Allende type B CAIs could result in such multiple heating processes. A possible candidate for an energy source for the multiple heating events would be an active protosun (17).
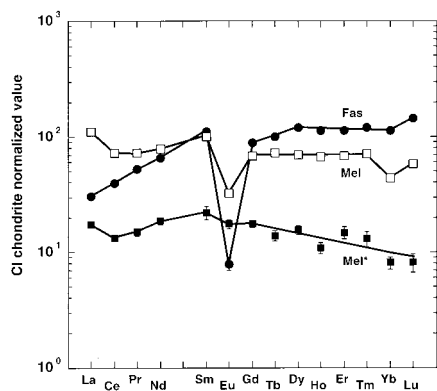
Fig. 3. Chondrite-normalized rare earth elements distribution of minerals in 7R-19-1 CAI. Measurements were performed with a modified ims 3f SIMS instrument of TiTech with the energy filtering technique (band-pass energy: 50 to 70 eV) with a primary beam size of ~20 μm in diameter. Locations of the SIMS analysis for Fas, Mel, and Mel* correspond to those for the points of F7, M12, and M4 in Fig. 1, respectively. Standard deviations determined by secondary-ion intensity statistics are shown as error bars if the error bars are greater than the symbol size. Further details of the analytical procedure have been described elsewhere (18).
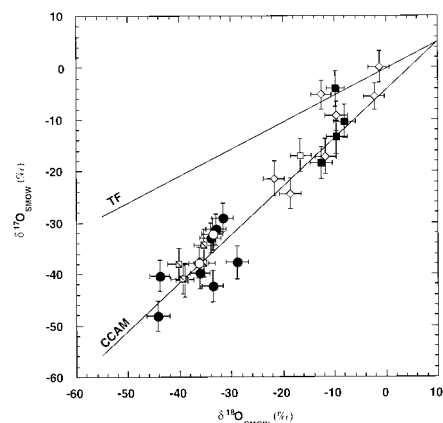
Fig. 4. Oxygen isotopic compositions of the 7R-19-1 CAI from the Allende meteorite. The mineral grains in Fig. 1 show large ^{16}O enrichments with the order of a melilite grain Mel* (solid circles), spinel grains (squares with an oblique line), a fassaite grain Fas (open diamond), and a melilite grain Mel (solid squares). The melilite grains of Mel* and Mel are in direct contact with each other. Fine fassaite grains trapped in Mel* (open circles) and in Mel (open square) show similar ^{16}O enrichment to the surrounding melilite grain, respectively. All data plot approximately along the CCAM line defined by (6). The terrestrial fractionation (TF) line is also shown. Errors are 1σ.

References and Notes

1. W. Boynton, in *Protostars and Planets II*, D. Black and M. Matthews, Eds. (Univ. of Arizona Press, Tucson, 1985), pp. 772–787; A. P. Boss, *Science* **241**, 565 (1988).
2. E. Stolper, *Geochim. Cosmochim. Acta* **46**, 2159 (1982).
3. G. J. MacPherson, D. A. Wark, J. T. Armstrong, in *Meteorites and the Early Solar System*, J. F. Kerridge and M. S. Matthews, Eds. (Univ. of Arizona Press, Tucson, 1988), pp. 746–807.
4. H. Nagasawa *et al.*, *Geochim. Cosmochim. Acta* **41**, 1587 (1977).
5. R. N. Clayton, N. Onuma, L. Grossman, T. K. Mayeda, *Earth Planet. Sci. Lett.* **34**, 209 (1977).
6. R. N. Clayton, *Annu. Rev. Earth Planet. Sci.* **21**, 115 (1993).
7. $\delta^{17 \text{ or } 18}O_{SMOW} = \{[(^{17 \text{ or }} {}^{18}O/ {}^{16}O)_{sample}/ (^{17 \text{ or }} {}^{18}O/^{16}O)_{SMOW}] - 1\} \times 1000$ [per mil], where SMOW indicates the standard mean ocean water.
8. R. N. Clayton and T. K. Mayeda, *Geophys. Res. Lett.* **4**, 295 (1977).
9. H. Yurimoto, M. Morioka, H. Nagasawa, *Geochim. Cosmochim. Acta* **53**, 2387 (1989); H. Yurimoto *et al.*, *Antarct. Meteorites XVI*, 60 (1991); F. J. Ryerson and K. D. McKeegan, *Geochim. Cosmochim. Acta* **58**, 3713 (1994).
10. K. D. McKeegan, L. A. Leshin, S. S. Russell, G. J. MacPherson, *Science* **280**, 414 (1998).
11. H. Yurimoto, H. Nagasawa, Y. Mori, O. Matsubaya, *Earth Planet. Sci. Lett.* **128**, 47 (1994).
12. S. B. Simon, A. M. Davis, L. Grossman, *Lunar Planet Sci.* **XXVI**, 1303 (1995).
13. The polished sample was coated with 30 nm of gold film for SIMS analysis to eliminate the electrostatic charge on the sample surface. Oxygen isotope ratios were measured with a modified Cameca ims 1270 SIMS of TiTech with a high mass resolution technique. The primary ion beam was mass filtered positive Cs ions accelerated to 10 keV and the beam spot size was ~3 μm in diameter. The primary current was adjusted for each measurement to obtain the count rate of negative ^{16}O ions of ~4 × 10⁵ cps. A normal-incident electron gun was utilized for charge compensation of the analysis area. Negative secondary ions from the ^{16}O tail, ^{16}O, ^{17}O, ^{16}OH and ^{18}O were analyzed at a mass resolution power of ~6000, sufficient to completely eliminate hydride interference. Secondary ions were detected by an electron multiplier operated in a pulse counting mode, and analyses were corrected for dead time (21 ns). The matrix effect which may cause inter-mineral systematic errors can be checked by comparing the analytical results for terrestrial analogues. We measured oxygen isotope ratios of terrestrial standards with known oxygen isotopic ratio (*11*), SPU (spinel from Russia), anorthite (Miyake-jima, Japan), augite (Takashima, Japan), synthetic gehlenite and synthetic åkermanite. The reproducibility of $^{17 \text{ or } 18}O/^{16}O$ on different analysis points of the same standard was ~5 per mil (1σ). The matrix effect of O isotopic analysis among these minerals was less than 5 per mil (1σ) under our analytical conditions. Therefore, we used the SPU standard to obtain O isotope ratio of all the CAI minerals. Overall errors in the measurements are estimated to be ~ 5 per mil (1σ) for each analysis. An average isotope ratio of the SPU standard was used to determine $\delta^{17 \text{ or } 18}O_{SMOW}$ values for corresponding unknown samples. The δ^{17} or $^{18}O_{SMOW}$ values were calculated as follows:

$$(\delta^{17 \text{ or } 18}O_{SMOW})_{uk} = (\delta^{17 \text{ or } 18}O_{SMOW})_{st} +$$
$$(R_{uk}/R_{st} - 1) \times 1000 \text{ [per mil]}$$

where R is the measured isotope ratio of $^{17 \text{ or } 18}O/ {}^{16}O$ and subscripts uk and st correspond to unknown and standard samples, respectively. Further details of the analytical procedure and the results will be given elsewhere (M. Ito *et al.*, in preparation). After SIMS analyses, the purity of analyzing area was evaluated by high magnification scanning electron microscopy and by optical microscopy. No submicron phases (such as submicron spinel grains or alteration products) were observed in the sputtered craters of the Cs⁺ primary beam.
14. Oxygen-16–enriched melilite grains that were not in contact with normal melilite grain were observed in a coarse-grained CAI from the Allende carbonaceous chondrite [G. L. Kim, H. Yurimoto, S. Sueno, *Lunar and Planet. Sci.* **XXIX**, abstr. 1344, Lunar and Planetary Institute, Houston, CD-ROM (1998)], in fine-grained CAIs from the Semarkona ordinary chondrite (*10*), from the ALH85085 ungrouped chondrite [M. Kimura, A. ElGoresy, H. Palme, E. Zinner, *Geochim. Cosmochim. Acta* **57**, 2329 (1993)], and in an Antarctic micrometeorite [C. Engrand, K. D. McKeegan, L. A. Leshin, *Meteoritics Planet. Sci.* **32**, A39 (1997)].
15. G. P. Meeker, *Meteoritics* **30**, 71 (1995).
16. J. P. Greenwood and P. C. Hess, in *Chondrules and the Plotoplanetary Disk*, R. H. Hewins, R. H. Jones, E. R. D. Scott, Eds. (Cambridge Univ. Press, Cambridge, UK, 1996), pp. 205–211.
17. F. H. Shu, H. Shang, A. E. Glassgold, T. Lee, *Science* **277**, 1475 (1997).
18. H. Yurimoto, A. Yamashita, N. Nishida, S. Sueno, *Geochem. J.* **23**, 215 (1989).
19. We thank E. King for providing 7R-19-1 CAI. Supported by the Kagaku-Gijutsu-Cho and the Monbu-Sho.

10 August 1998; accepted 29 October 1998

Single-Molecule Enzymatic Dynamics

H. Peter Lu, Luying Xun, X. Sunney Xie*

Enzymatic turnovers of single cholesterol oxidase molecules were observed in real time by monitoring the emission from the enzyme's fluorescent active site, flavin adenine dinucleotide (FAD). Statistical analyses of single-molecule trajectories revealed a significant and slow fluctuation in the rate of cholesterol oxidation by FAD. The static disorder and dynamic disorder of reaction rates, which are essentially indistinguishable in ensemble-averaged experiments, were determined separately by the real-time single-molecule approach. A molecular memory phenomenon, in which an enzymatic turnover was not independent of its previous turnovers because of a slow fluctuation of protein conformation, was evidenced by spontaneous spectral fluctuation of FAD.

Recent advances in fluorescence microscopy have allowed studies of single molecules in an ambient environment (*1, 2*). Single-molecule measurements can reveal the distribution of molecular properties in inhomogeneous systems (*3–10*). The distributions, which can be either static (*3–7*) or dynamical (*8–10*), cannot usually be determined by ensemble-averaged measurements. Moreover, stochastic trajectories of a single-molecule property can be recorded in real time, containing detailed dynamical information extractable through statistical analyses. Single-molecule trajectories of translational diffusion (*11–13*), rotational diffusion (*14*), spectral fluctuation (*15*), conformational motion (*16*), and photochemical changes (*17, 18*) have been demonstrated. Of particular interest is the real-time observation of chemical reactions of biomolecules. Enzymatic turnovers of a few motor protein systems have been monitored in real time (*19–21*). In the study reported here, we examined enzymatic turnovers of single flavoenzyme molecules by monitoring the fluorescence from their active sites. Statistical analyses of chemical dynamics at the single-molecule level revealed insights into enzymatic properties.

Flavoenzymes are ubiquitous and undergo redox reactions in a reversible manner (*22*). Cholesterol oxidase (COx) from *Brevibacterium* sp. is a 53-kD flavoenzyme that catalyzes the oxidation of cholesterol by oxygen (*23*) (Scheme 1). The active site of the enzyme (E) involves a flavin adenine dinucleotide (FAD), which is naturally fluorescent in its oxidized form but not in its reduced form. The FAD is first reduced by a cholesterol molecule to $FADH_2$, and is then oxidized by O_2, yielding H_2O_2. The crystal structure of COx (*23*) shows that the FAD is noncovalently and tightly bound to the center of the protein and is surrounded by a hydrophobic binding pocket for cholesterol, which is otherwise filled with 14 water molecules.

A fluorescence image of single COx molecules in their oxidized form (Fig. 1A) was taken with an inverted fluorescence microscope by raster-scanning the sample with a fixed He-Cd laser (442 nm, LiCONiX) focus
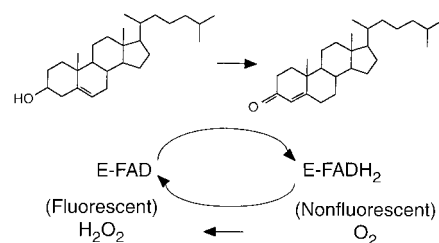
H. P. Lu and X. S. Xie, Pacific Northwest National Laboratory, William R. Wiley Environmental Molecular Sciences Laboratory, Richland, WA 99352, USA. L. Xun, Washington State University, Department of Microbiology, Pullman, WA 99164, USA.

*To whom correspondence should be addressed. E-mail: xsxie@pnl.gov

Scheme 1.